Optical spectroscopy of graphene: From the far infrared to the ultraviolet

Kin Fai Mak [a], Long Ju [b], Feng Wang [b,c,*], Tony F. Heinz [a,**]

[a] *Departments of Physics and Electrical Engineering, Columbia University, New York, NY 10027, USA*
[b] *Department of Physics, University of California at Berkeley, Berkeley, CA 94720, USA*
[c] *Materials Science Division, Lawrence Berkeley National Laboratory, Berkeley, CA 94720, USA*

ABSTRACT

The unique electronic structure of graphene leads to several distinctive optical properties. In this brief review, we outline the current understanding of two general aspects of optical response of graphene: optical absorption and light emission. We show that optical absorption in graphene is dominated by intraband transitions at low photon energies (in the far-infrared spectral range) and by interband transitions at higher energies (from mid-infrared to ultraviolet). We discuss how the intraband and interband transitions in graphene can be modified through electrostatic gating. We describe plasmonic resonances arising from the free-carrier (intraband) response and excitonic effects that are manifested in the interband absorption. Light emission, the reverse process of absorption, is weak in graphene due to the absence of a band gap. We show that photoluminescence from hot electrons can, however, become observable either through femtosecond laser excitation or strong electrostatic gating.

© 2012 Elsevier Ltd. All rights reserved.

1. Introduction

The two-dimensional graphene crystal exhibits fascinating electrical, mechanical, and optical properties. In this brief review, we examine the distinctive behavior of light-matter interactions in graphene. These interactions are surprisingly strong, rendering optical spectroscopy a powerful tool for probing the unusual physics of graphene. Indeed, it was the strong optical absorption of single-layer graphene (with its absorbance of $\sim$2.3% [1–7], as discussed below) that permitted the initial discovery of exfoliated monolayers by visual inspection under an optical microscope [8].

Here we describe investigations of optical absorption and emission in graphene, and how these processes can be modified through electrical gating. In addition to the fundamental interest inherent in such studies, a good understanding of the optical properties also helps to pave the way for novel photonics and optoelectronics applications of the material [9–13]. Our discussion highlights investigations of the authors and their colleagues. Because of limitations of space, this paper unfortunately cannot provide a full description of all related investigations.

2. Review of electronic structure of graphene

Graphene consists of a single layer of carbon atoms arranged in a honeycomb lattice structure, as defined by the sp^2 bonding. The electronic states of importance for the optical properties of graphene arise from the additional electron in the p_z orbitals of the carbon atoms [14–16]. These orbitals overlap to form bonding and antibonding states and the corresponding extended π-bands of graphene. Here we briefly describe the resulting electronic structure, with an emphasis on those properties critical for determining the optical response.

As a result of the symmetry between the A and B sublattices (Fig. 1(a)), the conduction and valence states in graphene are degenerate at the K and K′ points of the Brillouin zone (Fig. 1(b)) [15]. This degeneracy gives rise to a linear dispersion of the electronic bands [15–18]. Electrons near the two inequivalent valleys in graphene thus behave as massless Dirac Fermions and are characterized by a velocity of $v_F \sim 10^8$ cm s^{-1} [17,18]. Because of spatial inversion and time reversal symmetries, electrons at the K and K′ points are, in fact, 8-fold degenerate [19,20]. This degeneracy reflects the valley and spin degrees of freedom, as well as the band degeneracy that we have just introduced. In the vicinity of the K and K′ points, the 2D energy dispersion relation is isotropic in character and is known as the Dirac cone (Fig. 1(b)) [16–18,21,22].

Further away from these two valleys, trigonal warping modifies the 2D equi-energy contours (Fig. 1(c)) [16,23,24], reflecting the hexagonal lattice symmetry of the underlying graphene crystal. Moving still further from the K and K′ points, there is a

* Corresponding author at: Department of Physics, University of California at Berkeley, Berkeley, CA 94720, USA. Tel.: +510 643 3275.
** Corresponding author: Tel.: +212 854 6564.
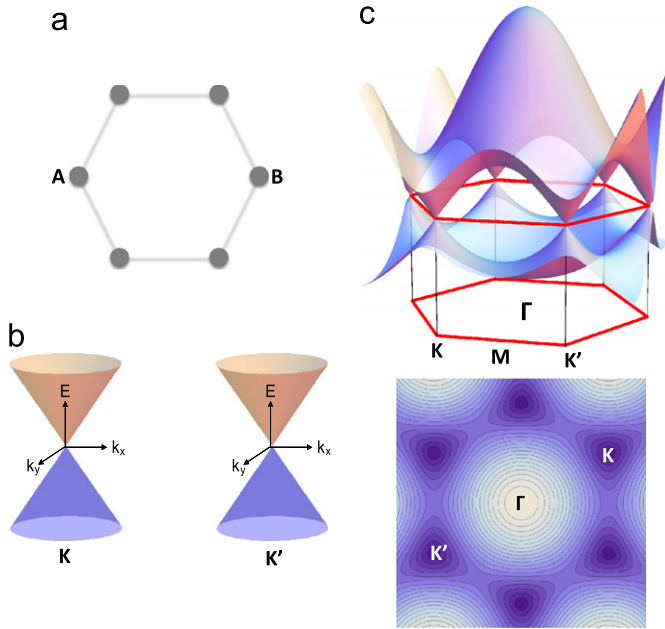*E-mail addresses:* fengwang76@berkeley.edu (F. Wang), tony.heinz@columbia.edu (T.F. Heinz).

Fig. 1. (Color online) Electronic structure of graphene: (a) the honeycomb lattice structure of graphene with the two inequivalent sites A and B occupied by carbon atoms, (b) the exact energy degeneracy at the K and K′ points of the Brillouin zone guarantees a linear energy-momentum dispersion (the massless spectrum of the Dirac cone) near the two inequivalent valleys, (c) the full electronic dispersion of the π-bands in the graphene Brillouin zone, showing the trigonal warping effects away from the K- and K′-points and the saddle point singularity at the M-point. The equi-energy contour lines of the conduction band are also displayed.

saddle-point singularity in the electronic bands at the M-point (Fig. 1(c)) [16,23,24]. Here electrons moving along the M–K (M–Γ) direction possess negative (positive) band masses. At the Γ-point, the conduction and valence π-electron states are widely separated, with a gap of ∼20 eV [16,23–26]. The equi-energy contour near the Γ-point is, like that of the K-point, isotropic in character, but exhibits parabolic dispersion.

The basic features of the electronic structure of graphene are captured by a simple tight-binding model that takes into account only the nearest neighbor couplings [16,23,24]. For a more accurate description of the π-band dispersion in graphene, one needs to include next-nearest neighbor couplings within a tight-binding model [26] or apply *ab-initio* methods, such as LDA+GW calculations [27–29].

3. Light absorption in graphene

The optical absorption of graphene arises from two distinct types of contributions, those from intraband and those from interband optical transitions [2,30]. The relative importance of the two contributions depends largely on the spectral range of interest. Here we review recent investigations of absorption of graphene over a wide spectral range, from the far infrared to the ultraviolet. In the far-infrared region, the optical response is dominated by the free-carrier (or intraband) response [2,30]. This contribution can be described to a good approximation by a Drude model [31]. By fabricating sub-wavelength structures in graphene, one can create a tunable far-infrared response that is dominated by plasmonic excitations associated with these free carriers [32]. In the mid- to near-infrared region, the optical absorbance is attributable primarily to interband transitions [30]. This response is nearly frequency independent and is equal to a universal value determined by the fine-structure constant $e^2/\hbar c$ in pristine graphene [1–7]. However, this optical absorption in

graphene can be controlled through electrostatic gating, which shifts the Fermi energy and induces Pauli blocking of the optical transitions [33,34]. In the ultraviolet spectral range (with the transitions approaching the saddle-point singularity), the interband optical absorption increases well beyond the "universal" value and exhibits signatures of excitonic effects [35–37]. In the following, we discuss separately the basic optical properties of graphene for low photon energies, where the intraband response dominates, and for higher photon energies, where the interband response dominates.

3.1. Intraband optical absorption

3.1.1. Free-carrier absorption

Since the speed of light c is much higher than the Fermi velocity v_F of graphene ($c/v_F \sim 300$) [17], direct absorption of a photon by an intraband optical transition does not satisfy momentum conservation. To conserve momentum, extra scattering with phonons or defects, as shown in Fig. 2(a), is required. The simplest description of the optical response of free carriers is then captured by a Drude model for the frequency-dependent sheet conductivity [30,38]

$$\sigma(\omega) = \frac{\sigma_0}{1 + i\omega\tau}. \tag{1}$$

Here σ_0 and τ denote, respectively, the dc conductivity and the electron scattering time, and ω represents the (angular) frequency of the light. (Note that the optical absorbance at normal incidence is related to optical sheet conductivity by $A(\omega) = (4\pi/c)Re[\sigma(\omega)]$.) To express the Drude conductivity in terms of microscopic material parameters, it is often convenient to introduce the Drude weight $D = \pi\sigma_0/\tau$, corresponding to the integrated oscillator strength of free carrier absorption. In conventional semiconductors or metals the Drude weight is given by $D = (\pi n e^2/m) = (\omega_p^2)/4$, with n and m denoting, respectively, the carrier density and carrier band mass, and ω_p the plasma frequency [39]. For graphene with its massless electrons, the Drude weight assumes a completely different form: $D = e^2 v_F \sqrt{\pi n}$ [1,16,30,38,40–42].

Far-infrared spectroscopy can be used to probe the intraband absorption in large-area graphene grown by chemical vapor deposition (CVD) [43,44]. In Fig. 2(b) we show the free-carrier absorption spectra of graphene at different doping levels [31]. These spectra can be fit reasonably well by the Drude form, consistent with theoretical calculations based on the Kubo formalism that ignore many-body interactions [2,30,38]. The Drude scattering rates for different gate voltages are shown in Fig. 2(c). The different electron and hole scattering rates suggest that they experience different defect potentials. Near charge neutrality, we observe a Drude scattering rate of $\sim 100\ cm^{-1}$, which corresponds to a momentum relaxation lifetime of ~ 50 fs.

From the Drude fit of the spectra in Fig. 2(b), we can obtain the free-carrier (or intraband) absorption Drude weight D_{intra}. This can be compared to the value $D_{inter} = e^2 v_F \sqrt{\pi n} = (e^2/\hbar)\epsilon_F$ [1,16,30,38,40–42], where the Fermi energy ϵ_F is determined from inspection of Pauli blocking of the interband absorption (as discussed below). As can be seen in Fig. 2(d), the observed intraband transition Drude weight, D_{intra}, yields a somewhat lower value than D_{inter}. We note that the Drude weight of intraband absorption should equal the reduction of interband absorption oscillator strength, as required by the sum rule. This is confirmed in Fig. 2(e). The measured reduction in D_{intra} is, therefore, correlated to the imperfect Pauli blocking of interband transitions at energies below $2\epsilon_F$ [33], as shown in Fig. 2(b). Modification of the free-carrier Drude conductivity can arise from impurity and defect states or from many-body interactions
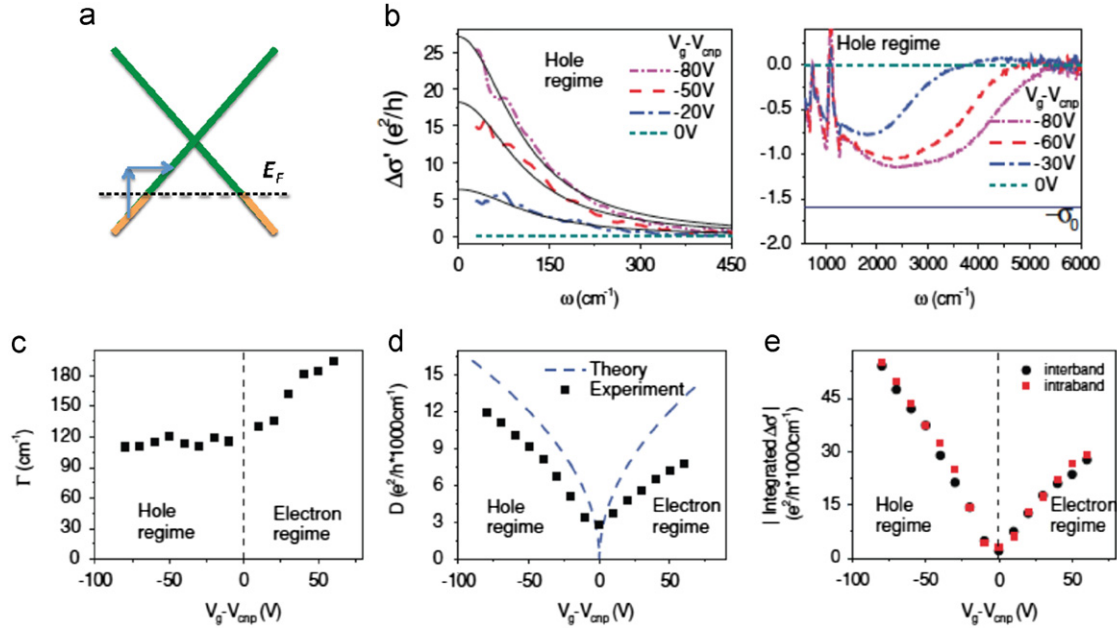
Fig. 2. (Color online) Free-carrier absorption in graphene (figures adapted from ref. [31]): (a) schematic representation of the intraband absorption process. To conserve momentum, scattering with phonons or defects is needed, (b) change in the optical sheet conductivity of graphene in the infrared range induced by electrostatic doping. In the far infrared, the conductivity is well described by the Drude model. In the mid to near infrared, Pauli blocking of interband transitions can be used to determine the Fermi energy, (c) the inferred Drude scattering rate as a function of gating voltage, (d) Drude weight as a function of gating voltage. We see that the measured Drude weight from the free-carrier response is suppressed with respect to the value predicted by $D_{inter} = (e^2/h)\epsilon_F$, (e) the integrated value of the change in optical sheet conductivity as a function of gating voltage. The change of the interband contribution is equal to that of the intraband parts, a consequence of the sum rule.
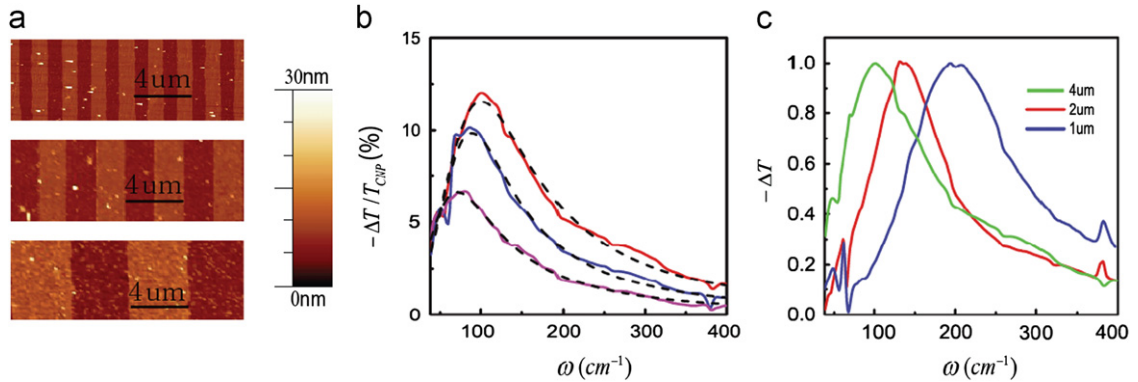

Fig. 3. (Color online) Plasmon excitations in graphene micro-ribbon arrays (figures adapted from ref. [32]): (a) images of samples with micro-ribbon widths (w) of 1, 2 and 4 μm, as determined by atomic-force microscopy, (b) control of the localized plasmon response through electrical gating. The far-infrared radiation was polarized perpendicular to the graphene ribbons. The plasmon resonance blue shifts and increases in amplitude as the doping level in graphene is increased, (c) change of transmission spectra for different graphene micro-ribbon widths at a constant doping level of 1.5×10^{13} cm^{-2}. All spectra are normalized by their respective peak values.

[45,46]. Yan et al. [47] recently showed that the degree of reduction of D_{intra} compared to D_{inter} was sample dependent. For samples with nearly perfect Pauli blocking of interband transitions, D_{intra} appears to be only slightly reduced at finite doping levels, consistent with theoretical calculations. High-quality graphene with low scattering rate will be required to probe the intrinsic behavior and possible many-body effects in the intraband absorption.

3.1.2. Plasmon excitations

Plasmons are quanta of collective oscillation of charge carriers. They are important for understanding the dynamic response of electron systems and for developing optical metamaterials [48–50]. Plasmons of Dirac electrons in graphene are predicted to exhibit behavior distinctly different not only from electrons in bulk

materials, but also from their counterparts in conventional 2D electron gas (2DEG) systems [46,51,52].

Direct light absorption by propagating plasmons in graphene film is not allowed due to the large momentum mismatch between photons and plasmons. However, plasmon absorption can be enabled with grating coupling, which provides an effective momentum due to the periodic grating structure. Alternatively, one can utilize *localized* plasmon resonances in graphene structures with sizes smaller than the relevant wavelengths. Ju *et al.* demonstrated that strong optical resonances from localized plasmons can be achieved in patterned arrays of graphene ribbons of micron widths (Fig. 3(a)) [32]. Standard photolithography and oxygen plasma etching were employed to prepare the required micro-ribbon array from large-area CVD graphene. The optical response of the graphene micro-ribbon arrays was probed using polarized Fourier-Transform Infrared Spectroscopy (FTIR). For light polarized along the length of the ribbon, the absorption spectrum is characterized by a Drude

response similar to that in bulk graphene sheets. For light polarized perpendicular to the length of the ribbon, however, prominent localized-plasmon resonances are observed (Fig. 3(b)). The coupling between light and the graphene plasmons is remarkably strong, with achievable oscillator strengths being an order of magnitude larger than that in conventional semiconducting 2DEGs [53,54]. This difference originates from a low effective electron mass and the much higher doping levels attainable in graphene.

The localized plasmon resonance in graphene can be modified through electrostatic doping. Fig. 3(b) shows the gate-dependent absorption associated with excitation of these localized plasmons. The plasmon resonance is seen to become stronger and its frequency to blue shift with increasing carrier density. The relation between the frequency of the plasmon resonance and the carrier concentration is found to scale as $\omega_p \propto n^{1/4} \propto |\epsilon_F|^{1/2}$ [51]. This scaling law, contrary to the $n^{1/2}$ dependence for conventional 2DEGs [53,54], is characteristic of Dirac electrons.

One can control the localized plasmon resonance by modifying the spatial patterning of graphene array. Fig. 3(c) displays the plasmon resonances in graphene micro-ribbons with different widths, but the same carrier concentration. We see that the plasmon frequency increases with decreasing ribbon width according to $\omega_p \propto w^{-1/2}$. Unlike the variation with carrier density, this geometric scaling arises from electrostatics and is obeyed by plasmon excitations in other 2D electron systems [46,51].

3.2. Interband optical absorption

3.2.1. Universal optical conductivity

Interband absorption arises from direct optical transitions between the valence and conduction bands (Fig. 4(a)). At frequencies above the far-infrared region, these interband transitions typically define the optical response of graphene. Within the tight-binding model, the optical sheet conductivity from interband transitions can be readily calculated [1–4,30,55,56]. For pristine graphene at zero temperature, the optical conductivity in the linear dispersion regime of graphene is found to be independent of frequency. The associated "universal" conductance of graphene is determined solely by fundamental constants and assumes the value of $\sigma(\omega) = \pi e^2/2h$ [1–4,6,7,30,38,55,56]. This conductivity corresponds to an absorbance of $A(\omega) = (4\pi/c)\sigma(\omega) = \pi\alpha \approx 2.29\%$ [6,7], where α denotes the fine structure constant.

The independence of the interband optical absorption on both frequency and the material properties (as encoded in the Fermi velocity v_F) can be understood in several ways. In general terms, it can be explained by dimensional analysis, since the graphene Hamiltonian describing the linear bands has no intrinsic energy scale with which to compare with the photon energy. More directly, in terms of a calculation of the absorption in perturbation theory, we note the perfect cancelation of the ω and v_F dependence in the three important parameters – the square of the transition matrix element ($\propto v_F^2/\omega^2$), the joint density of states ($\propto \omega/v_F^2$), and the photon energy ($\propto \omega$) – the product of which defines the optical absorption.

How does the predicted universal absorbance compare with experiment? Fig. 4(b) shows the frequency-dependent absorbance for three different graphene samples for photon energies between 0.5 and 1.2 eV. Over this spectral range, different samples show equivalent responses, not influenced by the detailed nature of the sample or its environment. Moreover, the absorbance is largely frequency independent, with an averaged value over the specified spectral range of $A = (2.28 \pm 0.14)\%$,
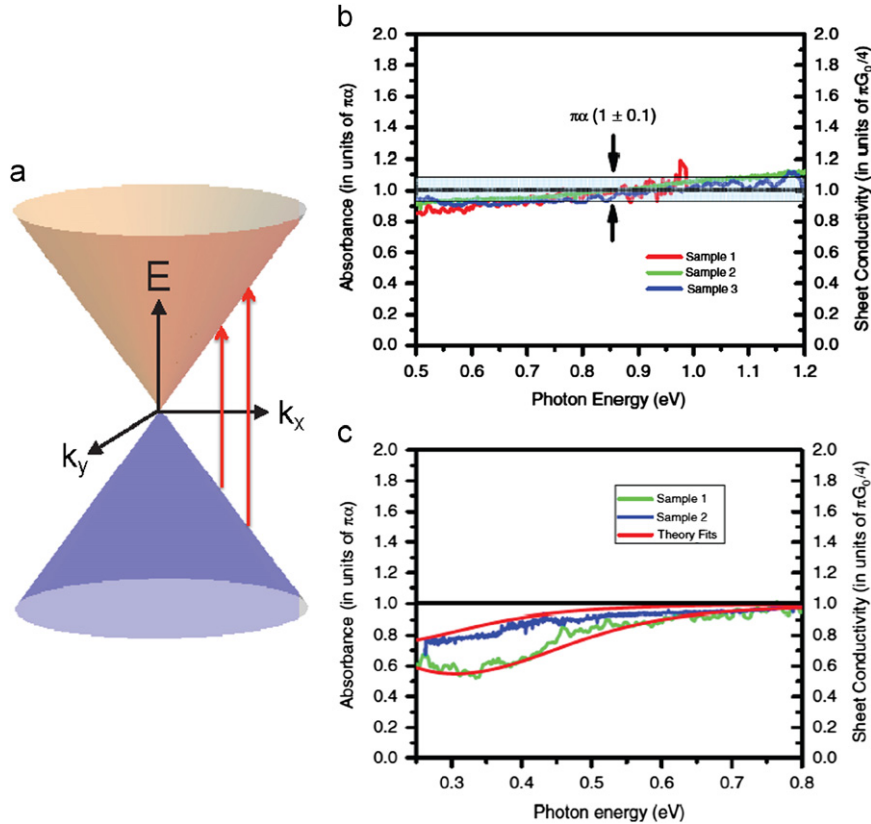

Fig. 4. (Color online) Universal optical sheet conductivity of graphene (figures adapted from ref. [6]): (a) schematic of interband optical transitions in graphene, (b) the optical sheet conductivity (in units of $\pi e^2/2h$, right scale) and the sheet absorbance (in units of $\pi\alpha$, left scale) of three different samples of graphene over the photon energy range of 0.5 to 1.2 eV. The black horizontal line corresponds to the universal value of $\pi\alpha = 2.293\%$ for the sheet absorbance, (c) the graphene sheet absorbance of sample 1 and 2 over a lower photon energy range of 0.25 to 0.8 eV. The smooth fits correspond to theory considering the presence of both finite temperatures and finite doping.
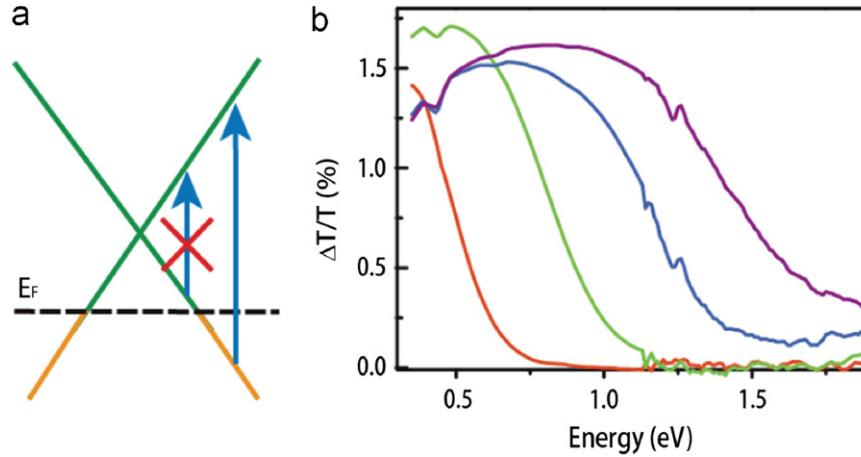
Fig. 5. (Color online) Gate-tunable interband transitions in graphene: (a) an illustration of interband transitions in hole-doped graphene. Optical transitions at photon energies greater than $2|\epsilon_F|$ are allowed, while those at energies below $2|\epsilon_F|$ are blocked, (b) the gate-induced change of transmission in hole-doped graphene as a function of gate voltage V_g. The values of the gate voltage referenced to that for charge neutrality, $V_g - V_{CNP}$, for the curves -0.75, -1.75, -2.75 and -3.5 V, from left to right.

consistent with the universal value of $\pi\alpha = 2.29\%$. The slight departure from a completely frequency-independent behavior, which becomes more pronounced at higher photon energies, will be discussed below.

We see, however, that this universal behavior does not hold well for a broader spectral range. Fig. 4(c), for example, displays the frequency-dependent absorbance for samples 1 and 2 for a lower range of photon energies. Below 0.5 eV the absorbance no longer conforms to the universal value, and it varies from sample to sample. This behavior arises from the presence of unintentional doping. For a graphene sample at temperature T with a chemical potential close to its Fermi energy ϵ_F, the frequency dependent optical sheet conductivity can be written as [30,56,57]

$$\sigma(\omega) = \frac{\pi e^2}{4h}\left[tanh\left(\frac{\hbar\omega + 2_F}{4k_BT}\right) + tanh\left(\frac{\hbar\omega - 2\epsilon_F}{4k_BT}\right)\right]. \quad (2)$$

As illustrated in Fig. 5(a), doping causes blocking of transitions for photon energies below $2|\epsilon_F|$, with the response somewhat broadened by the effect of finite temperature and carrier lifetime. From our experimental results, we conclude that sample 1 has a higher level of unintentional doping than sample 2. In addition to the unintentional doping naturally present in many samples, one can also control the carrier concentration through electrostatic gating. This allows one to investigate the doping-dependent interband transitions in graphene systematically, as we describe below.

3.2.2. Tunable interband optical transitions

Because of the single-atom thickness of graphene and its linear dispersion with a high Fermi velocity, the Fermi energy in graphene can be shifted by hundreds of meV through electrostatic gating. Such doping, as just discussed, leads to a strong change in the interband absorption through Pauli blocking. As incorporated in Eq. (2) and shown in Fig. 5(a), the interband transitions for photon energies below $2|\epsilon_F|$ are suppressed, while those at energies above $2|\epsilon_F|$ unaffected. The optical response in graphene thus becomes highly tunable.

In our experiment, the doping level is tuned electrostatically in a field-effect transistor (FET) configuration by applying gating voltage across a SiO_2 dielectric or an electrolyte layer. The doping concentration of the former structure is typically limited to $\sim 5 \times 10^{12}$ cm^{-2} by the breakdown of the oxide layer, while electrolyte gating can induce carrier concentrations as high as of 10^{14} cm^{-2} [58,59]. Fig. 5(b) displays change in the optical transmission as a function of photon energy induced using gating

with an ionic liquid electrolyte. Increased optical transmission arising from Pauli blocking is observed up to a threshold characterized by a photon energy of $2|\epsilon_F|$. With increased carrier doping, this threshold energy shifts to higher values, as expected. Using ionic liquid gating, one can reach a threshold energy above 1.7 eV, thus accessing the visible spectral range.

The tunability of the interband transitions in graphene offers new possibilities for probing fundamental physics and for various technological applications[33,34,60]. In addition, the underlying Pauli blocking process provides a direct approach to measuring the Fermi energy in graphene without the need of any electrical contacts. The threshold energy for increased optical absorption yields the value of $2|\epsilon_F|$, from which the carrier density $n = E_F^2/\pi\hbar^2 v_F^2$ can also be obtained.

3.2.3. Excitonic effects

As a semi-metal, one might intuitively expect that many-body effects would be weak in graphene. Indeed, the majority of the optical data in the infrared and the visible range can be satisfactorily explained in an independent particle picture. However, because of the single-atom thickness of graphene and the vanishing density of states at the Dirac point, screening of Coulomb interactions between charge carriers moving in the 2D plane is significantly reduced. Indeed, theoretical studies have predicted the influence of many-body effects on the optical properties of graphene, including deviations from the universal absorbance through a reduction in absorption at low photon energies [61] and the appearance of Fermi edge singularities [46,62]. While it is expected that improved measurements, particularly for well-defined carrier densities and reduced temperatures, will reveal such many-body corrections at relatively low photon energies, one clear and robust signature of many-body interactions in the optical spectra has already been identified experimentally. This is the behavior of the optical absorption near the saddle-point singularity at the M-point [35–37].

The frequency-dependent optical conductivity of graphene extending from the infrared to the ultraviolet (UV) range is shown in Fig. 6(a) [35]. In the UV range, we find that $\sigma(\omega)$ displays a pronounced and asymmetric peak at a photon energy of 4.62 eV. In the independent particle picture, the resonance feature at UV arises from band-to-band transitions near the saddle-point singularity at the M-point. Within this approximation, the spectral variation of $\sigma(\omega)$ in the vicinity of this peak should be determined essentially by the joint density of states (JDOS). For a 2D saddle-point at
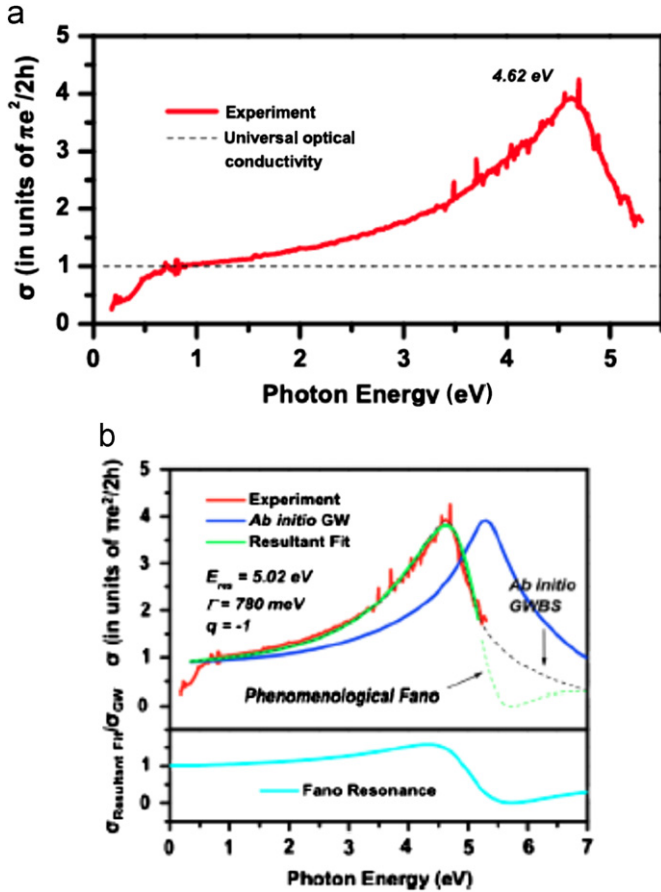
Fig. 6. (Color online) Excitonic effects on the optical absorption of graphene near the saddle-point singularity (figures adapted from ref. [35]): (a) the experimental optical sheet conductivity (solid line) and the universal value (dashed line) of graphene in the spectral range of 0.2 to 5.5 eV. The peak of absorbance is at 4.62 eV, (b) fit of experiment (red line) to the Fano model (green dashed line) presented in the text using the optical conductivity obtained from GW calculations (blue line) for the continuum background. The black dashed line is the optical conductivity obtained from the full GW–Bethe-Salpeter calculation [37]. The lower panel shows the Fano line shape of Eq. (3)

frequency ω_0, the JDOS is proportional to $-\log|1-(\omega/\omega_0)|$, which is essentially symmetric near the singularity [63]. Indeed, the sheet conductivity predicted within the framework of GW ab-initio calculations, shown in Fig. 6(b), does indeed display a symmetric peak [37]. Such GW calculations are known to provide an accurate description of the quasiparticle bands in graphene [27], but do not include the excitonic effects being considered here. In addition to the shape of the feature, the observed resonance is red shifted from the predicted GW peak position of $\hbar\omega_{GW}=5.20$ eV by almost 600 meV, over 10% of the saddle point energy [37].

The observed discrepancy can be explained by taking into account excitonic corrections to the optical response of graphene near the saddle-point singularity. Because of the absence of an energy gap in graphene, no stationary bound excitons can be formed. Instead, as predicted theoretically, the e–h interaction causes a redistribution of oscillator strengths from high to low photon energies [35,37]. This redistribution can be modeled by an exciton resonance at an energy below the saddle-point singularity that couples strongly with the existing continuum of electronic states [64–67]. Within a Fano model, we can express the resulting optical conductivity by

$$\frac{\sigma(\omega)}{\sigma_{GW}(\omega)} = \frac{(q+\varepsilon)^2}{1+\varepsilon^2}. \quad (3)$$

Here the GW sheet conductivity $\sigma_{GW}(\omega)$ is taken as the conductivity arising from band-to-band transitions without excitonic effects [37]; $\varepsilon=(\omega-\omega_{res})/(\Gamma/2)$ is photon energy relative to the resonance energy ω_{res} and normalized by width Γ; and q^2 reflects the ratio of the strengths of the excitonic transition to the band transitions, with the sign of q determining the asymmetry of the line shape. Such a coupled system leads to a red-shifted and asymmetric resonance feature [64–66], as shown by the fit to the experimental spectrum (green dashed line) in Fig. 6(b). We can also compare our measured spectrum with the earlier predictions of *ab-initio* GW–Bethe-Salpeter (GWBS) calculations that explicitly include the effect of e–h interactions (black dashed line) [37]. The agreement between theory and experiment is excellent. The fit to the experimental data, we note, incorporates a phenomenological broadening of the GWBS calculations by 200 meV. This accounts for the rapid decay of the excited states [68], which was not included in the calculation of the line shape.

The strong excitonic effects observed in the optical response of graphene reflect the reduced dielectric screening in a 2D system and the vanishing density of states at the Dirac point [51]. By doping graphene to a density above 10^{14} cm^{-2} [58], we produce a strong increase in the density of states at the Fermi level and more efficient screening of the Coulomb interactions between charge carriers. The influence of this change in carrier–carrier interactions on the saddle-point exciton has recently been observed [69]. Analysis of these effects not only yields a model of the optical response of doped graphene, but also information on both the fundamental aspects of many-body effects in graphene and the influence of doping on the lifetime and decay mechanisms of highly excited quasi-particles.

4. Light emission in graphene

Light emission by interband transitions is the reverse process of optical absorption. Since graphene, as discussed above, absorbs light very strongly through interband transitions, the question naturally arises is whether it can serve as an effective emitter of light. The answer to this question is that efficient light emission is impeded by carrier relaxation, which, because of the absence of a band gap, quickly brings the energy of highly excited e–h pairs down to low energies (Fig. 7(a)) [68,70–77]. As a result, the only widely investigated type of light emission from graphene is the inelastic scattering associated with phonon emission, *i.e.*, Raman scattering. The Raman process is very important for the study of phonons in graphene and, because of the role of electronic resonances, also for probing important aspects of the electronic structure [78–80]. This topic, and the extensive development of Raman spectroscopy for the characterization of graphene, is beyond the scope of this paper.

Here we focus on the less studied aspect of incoherent emission through photoluminescence (PL). PL is observable from both thermalized [70,71,81,82] and non-thermalized hot electrons [59] under appropriate circumstances. Spectroscopic study of such PL provides a useful analytic tool for investigation of the ultrafast relaxation and decoherence processes in graphene. We review our recent observations of light emission from graphene under two different regimes: (1) PL from thermalized hot electrons in pristine graphene under femtosecond laser excitation [70,71] and (2) hot PL from non-thermalized electrons in doped graphene under continuous-wave excitation [59]. Besides providing a fundamental understanding of the radiative recombination process in graphene, these studies also yield detailed information on its energy relaxation processes.
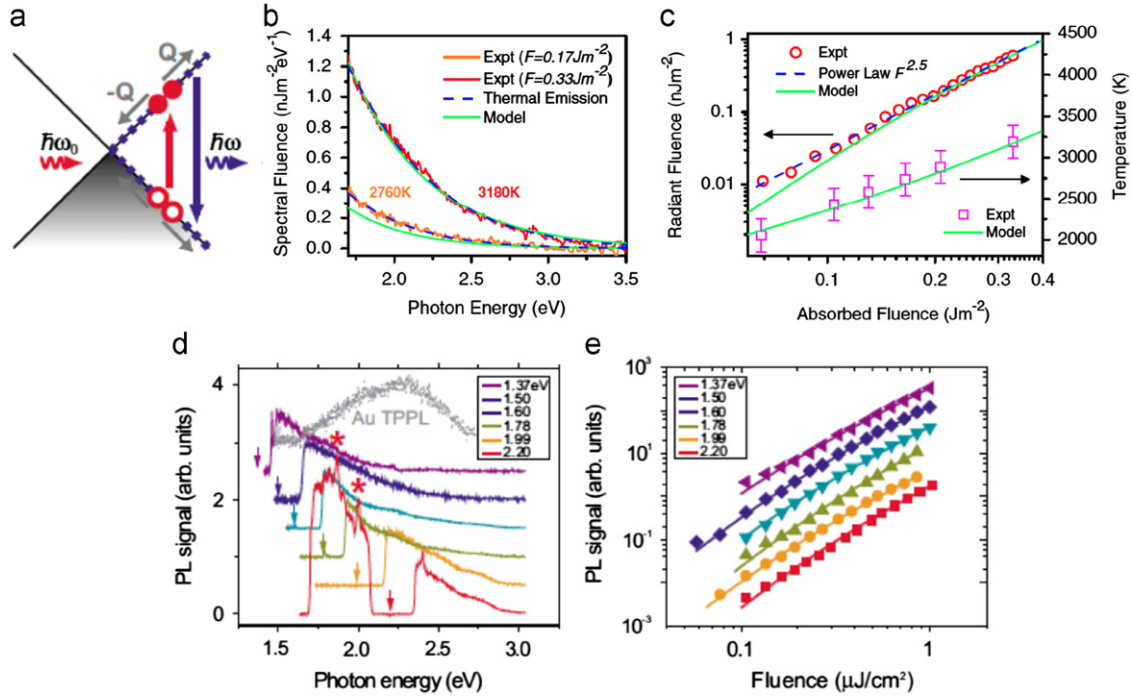
Fig. 7. (Color online) Ultrafast photoluminescence in graphene from thermalized hot electrons (figures adapted from refs. [70,71]): (a) schematic representation of the ultrafast PL process from interband recombination. Under the optical pump pulse excitation indicated by the red arrow, the electrons rapidly thermalize. They can then recombine to emit photons at higher energies than that of the pump photons, (b) spectral fluence of ultrafast PL from graphene at two different excitation fluences. The spectra are compatible with thermal emission described by Eq. (4) for T_{em}=2760 and 3180 K (blue dashed line), respectively, (c) light emission as a function of absorbed fluence. The red circles display experimental values for the integrated radiant fluence between 1.7 and 3.5 eV, which can phenomenologically be described by a power law with exponent of ~2.5 (blue dashed line). The magenta squares correspond to the experimental emission temperatures. The solid green lines in both (b) and (c) are fits based on a two-temperature model, (d) same as (b) under different excitation photon energies. The PL spectrum of gold is also shown for comparison, (e) the integrated radiant fluence for the blue-shifted emission as a function of pump fluence at different excitation energies, which can be described by a power law with exponents between 2 and 3.

4.1. Ultrafast emission from thermalized hot electrons

Pristine graphene under continuous-wave laser excitation exhibits no measurable light emission. In Fig. 7(b), we show, however, the readily measurable PL spectra from graphene when excited by 30-fs pulses from a Ti:sapphire laser [70]. The PL quantum yield is about 10^{-9}, more than 3 orders of magnitude greater than that obtained from the same sample under continuous-wave excitation, which falls below the detection threshold. A distinctive feature of the emission is its wide spectral range, extending over the visible to the near ultraviolet. In particular, the emission occurs at photon energies well above that of the incident pump photons (at 1.5 eV). This observation immediately excludes the possibility of conventional hot PL from non-thermalized charge carriers (to be discussed in the next section). Moreover, the integrated intensity over the blue-shifted PL spectral range exhibits a nonlinear fluence dependence, which can be described by a power law with exponent equal to 2.5 (Fig. 7(c)). Similar blue-shifted PL spectra are observed for different pump photon energies (Fig. 7(d)), all exhibiting a nonlinear dependence of the integrated intensity of the blue-shifted PL on laser fluence (Fig. 7(e)) [71].

The observed spectral radiant fluence $\mathcal{F}(\omega)$ and its nonlinear dependence on absorbed fluences can be understood within a model of thermal emission:

$$\mathcal{F}(\omega) = \tau_{em}e(\omega)\frac{\omega^3}{2\pi^2c^2}\left[\exp\left(\frac{\hbar\omega}{k_BT_{em}}\right)-1\right]^{-1} \quad (4)$$

Here τ_{em}, $e(\omega){=}A(\omega)$, and T_{em} denote, respectively, the effective emission time for each pulsed excitation, the emissivity, which is equal to the graphene absorbance, and the effective emission temperature of the charge carriers. We note that graphene is spectrally very close to an ideal blackbody over the specified

spectral range because of its largely frequency independent absorbance of $A(\omega) \approx \pi\alpha$ discussed above in Section 3.2. As shown in Fig. 7(b), the measured PL spectra can be fit well by this simple model; the inferred temperature T_{em} lies in the range of 2000–3200 K and varies sublinearly with pump fluence (Fig. 7(c)).

The above analysis shows that the electronic system in graphene rapidly thermalizes to a Fermi–Dirac distribution and achieves a high emission temperature T_{em} during a time scale of the laser pulse duration ~30 fs. This observation is consistent with the high rates of carrier relaxation inferred in the analysis of excitonic effects at the M-point (Section 3.2 above), as well as with recent theoretical and experimental investigations [68,70–77].

An interesting result emerges after consideration of the deposited energy in the excitation pulse and the resulting emission temperature. The observed range of emission temperatures for the given absorbed fluence lies between the two limiting cases for possible thermalization process: that of complete retention of absorbed energy within the electronic system and that of full equilibration of the electrons with all the lattice vibrational degrees of freedom. In the former case, the predicted temperature far exceeds the measured T_{em}, while in the latter case the predicted temperature rise is far too small. In fact, a partial equilibration with certain strongly coupled optical phonons (SCOPs, the highest energy phonons near the Γ- and K-point) needs to be invoked. To describe the process quantitatively, a two-temperature model involving the electron and the SCOP systems is used. Within the model, full equilibration between the two systems happens in a time scale ~50 fs, at which point ~95% of the absorbed optical energy resides in the SCOP system. Consequently the electronic temperature is strongly reduced and agrees with the range of measured values of T_{em}. The fluence dependence of the PL process can be understood within this model, as shown by the green curves in Fig. 7(b) and (c).

4.2. Emission from non-thermalized hot electrons

Upon excitation with a single photon, an energetic electron–hole pair is created in graphene. This electron and hole then relax independently through electron–electron and electron–phonon interactions on the ultrafast time scale. Before they reach equilibrium, the non-thermalized electron and hole have sufficient energy to emit a photon and generate hot-electron luminescence. This hot luminescence is usually very weak in solid-state materials, but can typically still be detected with modern cooled detectors. It can provide valuable information on the ultrafast dynamics of the excited state.

In pristine graphene, however, such photoluminescence has never been observed for cw excitation. The absence of any measurable hot PL reflects the fact that the hot electron and hot hole will almost immediately have different momenta because of their independent relaxation processes. Momentum conservation thus prevents them from recombining and emitting a photon.

In gated graphene, however, the situation can change dramatically. Fig. 8(a) shows a two-dimensional plot of the inelastic light emission spectrum as a function of electron doping (as characterized by the value of $2|\epsilon_F|$) [59]. Broadband hot-electron luminescence is observed with an intensity comparable to that of Raman processes when $2|\epsilon_F|$ approaches the laser excitation energy of 1.58 eV. A representative spectrum for the hot-electron luminescence at

$2|\epsilon_F| = 1.4$ eV, corresponding to a horizontal line-cut in Fig. 8(a), is presented in Fig. 8(b). The emergence of hot-electron luminescence can be understood by noting that a new radiative recombination channel opens up in the strongly doped graphene, as illustrated in Fig. 8(c): The hot electron, once it relaxes to an energy less then $|\epsilon_F|$, can readily undergo radiative recombination with a hole having the same momentum that is available in the strongly doped graphene. This picture implies that for a given Fermi level, hot-electron luminescence is possible only for photons at energies below $2|\epsilon_F|$. Indeed, as shown in Fig. 8(d), this is what we observe experimentally: For emission at higher photon energy, a larger threshold value for $2|\epsilon_F|$ is required.

5. Conclusions

This brief review has, we hope, served to illustrate the utility of photons in elucidating the response of graphene in different spectral regions, as well as our ability to control this response through electrostatic gating. At low frequencies, intraband transitions and the collective response of carriers through plasmons dominate the behavior, while interband transitions define the optical response at higher frequencies. Recent measurements have highlighted the importance of electron scattering by impurities and phonons (for the intraband transitions) and of electron–hole interactions (for the
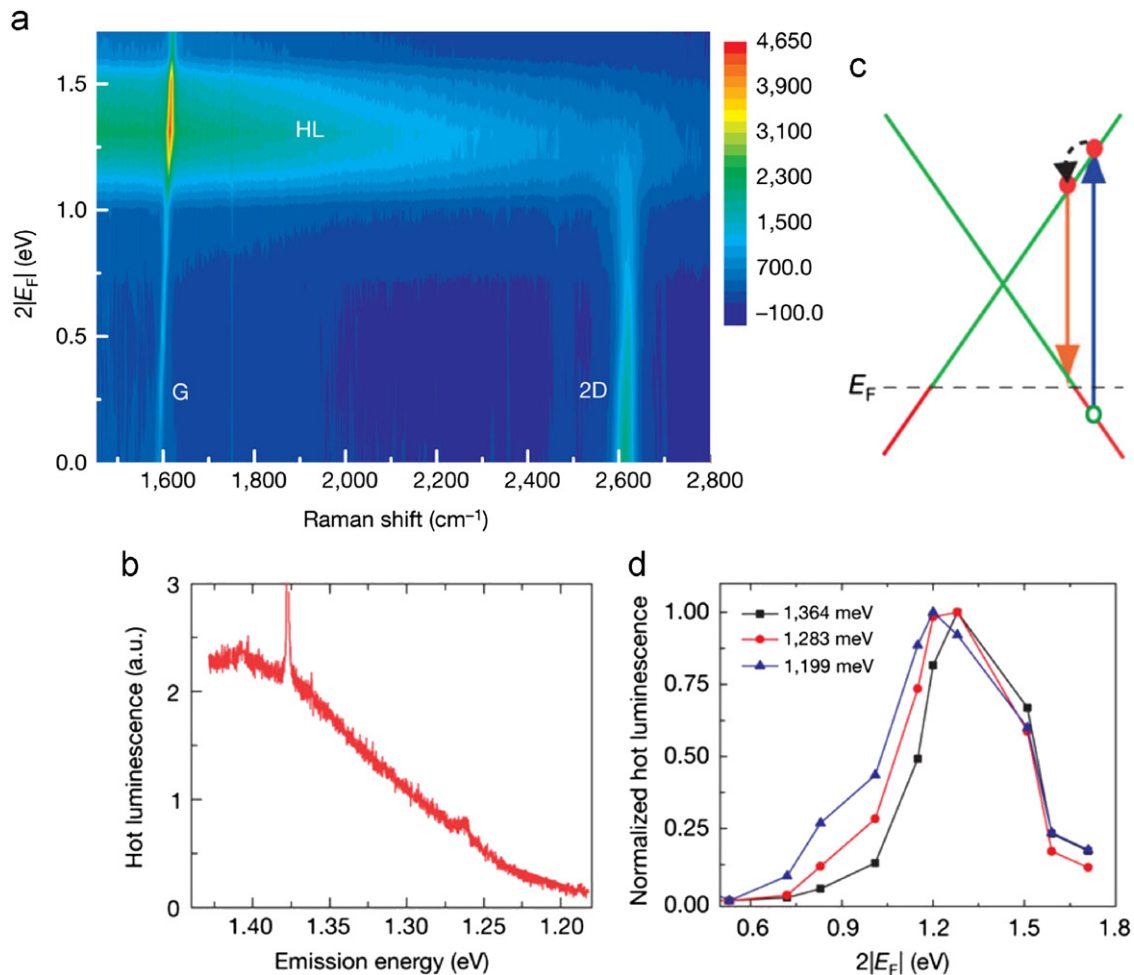

Fig. 8. (Color online) Hot PL in graphene from nonthermalized electrons (figures adapted from ref. [59]): (a) graphene inelastic light scattering intensity as a function of Stokes Raman shift and $2\epsilon_F$ for excitation at 1.58 eV photon energy. Besides the variation in intensities of the Raman G and 2D modes, a broad hot PL feature emerges as $2|\epsilon_F|$ approaches to the laser excitation energy, (b) the hot PL spectrum at $2|\epsilon_F| = 1.4$ eV has an integrated intensity more than 100 times stronger than from the Raman modes, (c) schematic representation of generation of hot PL. As $2|\epsilon_F|$ approaches the laser excitation energy: the probability for a hot electron (which relaxes very rapidly) to find a hole is dramatically enhanced, leading to the observed PL feature, (d) normalized PL intensity as a function of $2|\epsilon_F|$ for three different emission energies.

interband transitions) for a complete description of the optical response. The possibility for direct probing of such interactions in the time domain was illustrated in this review only through the example of light emission induced by femtosecond laser pulses. The wide range of ultrafast measurement techniques for pumping and probing graphene response from the THz to the UV are, however, being increasingly applied and are providing valuable information about the coupling of the different degrees of freedom of the system. Also of importance are careful measurements of line shapes of the graphene optical response, both in the region of intraband transitions and at the onset of interband transitions. Other promising future directions include characterization of the nonlinear optical response of single-layer graphene, which has not yet been performed in a systematic fashion, and the full extension of these diverse optical investigations to few-layer graphene samples.

Acknowledgment

References

[1] T. Ando, Y.S. Zheng, H. Suzuura, J. Phys. Soc. Jpn. 71 (2002) 1318–1324.
[2] V.P. Gusynin, S.G. Sharapov, J.P. Carbotte, Phys. Rev. Lett. 96 (2006) 256802.
[3] N.M.R. Peres, F. Guinea, A.H.Castro Neto, Phys. Rev. B 73 (2006) 125411.
[4] D.S.L. Abergel, V.I. Fal'ko, Phys. Rev. B 75 (2007) 155430.
[5] A.B. Kuzmenko, E. van Heumen, F. Carbone, D. van der Marel, Phys. Rev. Lett. 100 (2008) 117401.
[6] K.F. Mak, M.Y. Sfeir, Y. Wu, C.H. Lui, J.A. Misewich, T.F. Heinz, Phys. Rev. Lett. 101 (2008) 196405.
[7] R.R. Nair, P. Blake, A.N. Grigorenko, K.S. Novoselov, T.J. Booth, T. Stauber, N.M.R. Peres, A.K. Geim, Science 320 (2008) 1308.
[8] K.S. Novoselov, A.K. Geim, S.V. Morozov, D. Jiang, Y. Zhang, S.V. Dubonos, I.V. Grigorieva, A.A. Firsov, Science 306 (2004) 666–669.
[9] F. Bonaccorso, Z. Sun, T. Hasan, A.C. Ferrari, Nat. Photonics. 4 (2010) 611–622.
[10] N.M. Gabor, J.C.W. Song, Q. Ma, N.L. Nair, T. Taychatanapat, K. Watanabe, T. Taniguchi, L.S. Levitov, P. Jarillo-Herrero, Science 334 (2011) 648–652.
[11] J. Park, Y.H. Ahn, C. Ruiz-Vargas, Nano Lett. 9 (2009) 1742–1746.
[12] F. Xia, T. Mueller, R. Golizadeh-Mojarad, M. Freitag, Y.-m. Lin, J. Tsang, V. Perebeinos, P. Avouris, Nano Lett. 9 (2009) 1039–1044.
[13] X. Xu, N.M. Gabor, J.S. Alden, A.M. van der Zande, P.L. McEuen, Nano Lett. 10 (2009) 562–566.
[14] P.R. Wallace, Phys. Rev. 71 (1947) 622–634.
[15] J.C. Slonczewski, P.R. Weiss, Phys. Rev. 109 (1958) 272–279.
[16] A.H. Castro Neto, F. Guinea, N.M.R. Peres, K.S. Novoselov, A.K. Geim, Rev. Mod. Phys. 81 (2009) 109–162.
[17] Y.B. Zhang, Y.W. Tan, H.L. Stormer, P. Kim, Nature 438 (2005) 201–204.
[18] K.S. Novoselov, A.K. Geim, S.V. Morozov, D. Jiang, M.I. Katsnelson, I.V. Grigorieva, S.V. Dubonos, A.A. Firsov, Nature 438 (2005) 197–200.
[19] V.P. Gusynin, S.G. Sharapov, Phys. Rev. Lett. 95 (2005) 146801.
[20] E. McCann, V.I. Fal'ko, Phys. Rev. Lett. 96 (2006) 086805.
[21] A.K. Geim, K.S. Novoselov, Nat. Mater. 6 (2007) 183–191.
[22] A.K. Geim, Science 324 (2009) 1530–1534.
[23] R. Saito, G. Dresselhaus, M.S. Dresselhaus, Physical Properties of Carbon Nanotubes, Imperial College Press, London, 1998.
[24] S. Reich, C. Thomsen, J. Maultzsch, Carbon Nanotubes: Basic Concepts and Physical Properties, Wiley-VCH, Darmstadt, 2004.
[25] B. Partoens, F.M. Peeters, Phys. Rev. B 74 (2006) 075404.
[26] A. Grüneis, C. Attaccalite, L. Wirtz, H. Shiozawa, R. Saito, T. Pichler, A. Rubio, Phys. Rev. B 78 (2008) 205425.
[27] A. Grüneis, C. Attaccalite, T. Pichler, V. Zabolotnyy, H. Shiozawa, S.L. Molodtsov, D. Inosov, A. Koitzsch, M. Knupfer, J. Schiessling, R. Follath, R. Weber, P. Rudolf, L. Wirtz, A. Rubio, Phys. Rev. Lett. 100 (2008) 037601.
[28] C.-H. Park, F. Giustino, C.D. Spataru, M.L. Cohen, S.G. Louie, Nano Lett. 9 (2009) 4234–4239.
[29] P.E. Trevisanutto, C. Giorgetti, L. Reining, M. Ladisa, V. Olevano, Phys. Rev. Lett. 101 (2008) 226405.
[30] N.M.R. Peres, Rev. Mod. Phys. 82 (2010) 2673–2700.
[31] J. Horng, C.-F. Chen, B. Geng, C. Girit, Y. Zhang, Z. Hao, H.A. Bechtel, M. Martin, A. Zettl, M.F. Crommie, Y.R. Shen, F. Wang, Phys. Rev. B 83 (2011) 165113.
[32] L. Ju, B.S. Geng, J. Horng, C. Girit, M. Martin, Z. Hao, H.A. Bechtel, X.G. Liang, A. Zettl, Y.R. Shen, F. Wang, Nat. Nanotechnol. 6 (2011) 630–634.
[33] Z.Q. Li, E.A. Henriksen, Z. Jiang, Z. Hao, M.C. Martin, P. Kim, H.L. Stormer, D.N. Basov, Nat. Phys. 4 (2008) 532–535.
[34] F. Wang, Y.B. Zhang, C.S. Tian, C. Girit, A. Zettl, M. Crommie, Y.R. Shen, Science 320 (2008) 206–209.
[35] K.F. Mak, J. Shan, T.F. Heinz, Phys. Rev. Lett. 106 (2011) 046401.
[36] V.G. Kravets, A.N. Grigorenko, R.R. Nair, P. Blake, S. Anissimova, K.S. Novoselov, A.K. Geim, Phys. Rev. B 81 (2010) 155413.
[37] L. Yang, J. Deslippe, C.-H. Park, M.L. Cohen, S.G. Louie, Phys. Rev. Lett. 103 (2009) 186802.
[38] S. Das Sarma, S. Adam, E.H. Hwang, E. Rossi, Rev. Mod. Phys. 83 (2011) 407–470.
[39] N.W. Ashcroft, N.D. Mermin, Solid State Physics, Thomson Learning, USA, 1976.
[40] E.H. Hwang, S. Adam, S. Das Sarma, Phys. Rev. Lett. 98 (2007) 186806.
[41] K. Nomura, A.H. MacDonald, Phys. Rev. Lett. 98 (2007) 076602.
[42] N.M.R. Peres, J.M.B.L. dos Santos, T. Stauber, Phys. Rev. B 76 (2007) 073412.
[43] K.S. Kim, Y. Zhao, H. Jang, S.Y. Lee, J.M. Kim, K.S. Kim, J.H. Ahn, P. Kim, J.Y. Choi, B.H. Hong, Nature 457 (2009) 706–710.
[44] X.S. Li, W.W. Cai, J.H. An, S. Kim, J. Nah, D.X. Yang, R. Piner, A. Velamakanni, I. Jung, E. Tutuc, S.K. Banerjee, L. Colombo, R.S. Ruoff, Science 324 (2009) 1312–1314.
[45] D.N. Basov, R.D. Averitt, D. van der Marel, M. Dressel, K. Haule, Rev. Mod. Phys. 83 (2011) 471–541.
[46] S.H. Abedinpour, G. Vignale, A. Principi, M. Polini, W.-K. Tse, A.H. MacDonald, Phys. Rev. B 84 (2011) 045429.
[47] H. Yan, F. Xia, W. Zhu, M. Freitag, C. Dimitrakopoulos, A.A. Bol, G. Tulevski, P. Avouris, A.C.S. Nano 5 (2011) 9854–9860.
[48] H.T. Chen, W.J. Padilla, J.M.O. Zide, A.C. Gossard, A.J. Taylor, R.D. Averitt, Nature 444 (2006) 597–600.
[49] J.B. Pendry, A.J. Holden, W.J. Stewart, I. Youngs, Phys. Rev. Lett. 76 (1996) 4773–4776.
[50] T.J. Yen, W.J. Padilla, N. Fang, D.C. Vier, D.R. Smith, J.B. Pendry, D.N. Basov, X. Zhang, Science 303 (2004) 1494–1496.
[51] E.H. Hwang, S. Das Sarma, Phys. Rev. B 75 (2007) 205418.
[52] B. Wunsch, T. Stauber, F. Sols, F. Guinea, New J. Phys. 8 (2006) 318.
[53] E. Batke, D. Heitmann, C.W. Tu, Phys. Rev. B 34 (1986) 6951–6960.
[54] S.J. Allen, D.C. Tsui, R.A. Logan, Phys. Rev. Lett. 38 (1977) 980–983.
[55] M. Koshino, T. Ando, Phys. Rev. B 77 (2008) 115313.
[56] T. Stauber, N.M.R. Peres, A.K. Geim, Phys. Rev. B 78 (2008) 085432.
[57] M. Mecklenburg, J. Woo, B.C. Regan, Phys. Rev. B 81 (2010) 245401.
[58] D.K. Efetov, P. Kim, Phys. Rev. Lett. 105 (2010) 256805.
[59] C.F. Chen, C.H. Park, B.W. Boudouris, J. Horng, B.S. Geng, C. Girit, A. Zettl, M.F. Crommie, R.A. Segalman, S.G. Louie, F. Wang, Nature 471 (2011) 617–620.
[60] M. Liu, X.B. Yin, E. Ulin-Avila, B.S. Geng, T. Zentgraf, L. Ju, F. Wang, X. Zhang, Nature 474 (2011) 64–67.
[61] E.G. Mishchenko, Phys. Rev. Lett. 98 (2007) 216801.
[62] N.M.R. Peres, R.M. Ribeiro, A.H. Castro Neto, Phys. Rev. Lett. 105 (2010) 055501.
[63] F. Bassani, G.P. Parravincini, Electronic States and Optical Transitions in Solids, Pergamon Press, Oxford, 1975.
[64] J.C. Phillips, Phys. Rev. 136 (1964) A1705–A1713.
[65] E.O. Kane, Phys. Rev. 180 (1969) 852–858.
[66] P.Y. Yu, M. Cardona, Fundamentals of Semiconductors: Physics and Materials Properties, Springer, Berlin, 1996.
[67] U. Fano, Phys. Rev. 124 (1961) 1866–1878.
[68] C.-H. Park, F. Giustino, M.L. Cohen, S.G. Louie, Phys. Rev. Lett. 99 (2007) 086804.
[69] K.F. Mak, F. Jornada, N. Petrone, K. He, J. Hone, J. Shan, S.G. Louie, T.F. Heinz, in preparation.
[70] C.H. Lui, K.F. Mak, J. Shan, T.F. Heinz, Phys. Rev. Lett. 105 (2010) 127404.
[71] W.-T. Liu, S.W. Wu, P.J. Schuck, M. Salmeron, Y.R. Shen, F. Wang, Phys. Rev. B 82 (2010) 081408.
[72] D. Sun, Z.-K. Wu, C. Divin, X. Li, C. Berger, W.A. de Heer, P.N. First, T.B. Norris, Phys. Rev. Lett. 101 (2008) 157402.
[73] H. Wang, J.H. Strait, P.A. George, S. Shivaraman, V.B. Shields, M. Chandrashekhar, J. Hwang, F. Rana, M.G. Spencer, C.S. Ruiz-Vargas, J. Park, Appl. Phys. Lett. 96 (2010) 081917.
[74] J.M. Dawlaty, S. Shivaraman, M. Chandrashekhar, F. Rana, M.G. Spencer, Appl. Phys. Lett. 92 (2008) 042116.
[75] R.W. Newson, J. Dean, B. Schmidt, H.M. van Driel, Opt. Express 17 (2009) 2326–2333.
[76] P.A. George, J. Strait, J. Dawlaty, S. Shivaraman, M. Chandrashekhar, F. Rana, M.G. Spencer, Nano Lett. 8 (2008) 4248–4251.
[77] S. Kumar, M. Anija, N. Kamaraju, K.S. Vasu, K.S. Subrahmanyam, A.K. Sood, C.N.R. Rao, Appl. Phys. Lett. 95 (2009) 191911.
[78] A.C. Ferrari, Solid State Commun. 143 (2007) 47–57.
[79] M.A. Pimenta, G. Dresselhaus, M.S. Dresselhaus, L.G. Cancado, A. Jorio, R. Saito, Phys. Chem. Chem. Phys. 9 (2007) 1276–1291.
[80] L.M. Malard, M.A. Pimenta, G. Dresselhaus, M.S. Dresselhaus, Phys. Rep. Rev. Sect. Phys. Lett. 473 (2009) 51–87.
[81] S. Berciaud, M.Y. Han, K.F. Mak, L.E. Brus, P. Kim, T.F. Heinz, Phys. Rev. Lett. 104 (2010) 227401.
[82] M. Freitag, H.-Y. Chiu, M. Steiner, V. Perebeinos, P. Avouris, Nat. Nano 5 (2010) 497–501.